Applied Clay Science 204 (2021) 106019

Contents lists available at ScienceDirect

Applied Clay Science

journal homepage: www.elsevier.com/locate/clay

Research Paper

Preparation of high-performance silico-aluminophosphate geopolymers using fly ash and metakaolin as raw materials

Haozhe Guo [a,b], Baifa Zhang [a,b], Liangliang Deng [a,b], Peng Yuan [a,b,*], Mengyuan Li [a,b], Qiang Wang [a,b]

[a] CAS Key Laboratory of Mineralogy and Metallogeny/Guangdong Provincial Key Laboratory of Mineral Physics and Materials, Guangzhou Institute of Geochemistry, Institutions of Earth Science, Chinese Academy of Sciences, Guangzhou 510640, China
[b] University of Chinese Academy of Sciences, 19 Yuquan Road, Beijing 100049, China

ARTICLE INFO

Keywords:
Metakaolin
Fly ash
Phosphoric acid
Geopolymers

ABSTRACT

Silico-aluminophosphate (SAP) geopolymers were synthesized by using metakaolin (MK) and a high content of fly ash (FA) for the first time. With the increase in the FA mass fraction in the raw materials from 50% to 100%, the setting time of the SAP geopolymers was shortened and their compressive strength was decreased. The effects of the FA content on the SAP geopolymers composition and microstructure were investigated. The results showed that a high FA proportion caused the lack of active aluminum, which led to excess phosphate acid reacting with the calcium from FA. The fast formation of amorphous calcium phosphate (ACP) shortened the initial setting time through the consumption of water. However, after long-term aging, ACP transformed into needle- and slice-like nanoparticles, which decreased the compressive strength of the resulting geopolymers. Moreover, MK supplied active aluminum to increase the water-containing -Si-O-Al-O-P- network (SAP gel). The SAP gel contributed to the compressive strength enhancement and prevented the ACP transformation; however, it prolonged the final setting time, due to the slow polycondensation of SAP gel. These results indicate that a desirable setting time and compressive strength of the SAP geopolymers can be achieved by adjusting the FA and MK contents.

1. Introduction

Geopolymer, a novel inorganic polymer has been considered as an alternative to Portland cement because of its outstanding mechanical properties and eco-friendly characteristics (Font et al., 2018). Geopolymers can be produced from aluminosilicates sources under strong alkaline or acidic conditions. Alkali compounds are the most commonly used activators, including sodium hydroxide (Zhang et al., 2020a), potassium hydroxide, and sodium silicate (Tippayasam et al., 2016). The alkali activator depolymerize the aluminosilicate precursors into silicon-oxygen tetrahedrons ($[SiO_4]$) and aluminum-oxygen tetrahedron ($[AlO_4]$) monomers. Through the polycondensation of the monomers, disordered -Si-O-Al- three-dimensional structures with different Si/Al molar ratios can be formed (Davidovits, 1991). The structure carries the negative charges because of the Al in 4-fold coordination, which is charge-balanced by metal cations coming from the alkali activator and impurities in the raw material (Duxson et al., 2007). Geopolymers formed in this way are defined as alkali-aluminosilicate (AAS) geopolymers and have been widely applied in the fields of construction (Davidovits, 2017) and environmental protection, for several functions, such as adsorption and immobilization (Abdullah et al., 2017; Joussein et al., 2019). However, AAS geopolymers have some drawbacks; for example, the metal cations create deficiencies. The cations species and quantities result in unstable compressive strength and thermal stability of AAS geopolymers (van Jaarsveld and van Deventer, 1999; Bernal et al., 2015; Sellami et al., 2019). Moreover, in acidic media, hydrogen ions can readily replace the metal cations, which leads to structure deterioration (Bakharev, 2005).

Acid-activation is another route for geopolymers preparation. Phosphoric acid (H_3PO_4) is frequently used as an acid-activator (Liu et al., 2010; Louati et al., 2016a; Mathivet et al., 2019). Unlike alkali-activation, in acid activated geopolymerization, the phosphorus-oxygen tetrahedron ($[PO_4]$) participates in the polycondensation to form silico-aluminophosphate (-Si-O-Al-O-P-, SAP) network with water

* Corresponding author at: CAS Key Laboratory of Mineralogy and Metallogeny, Guangzhou Institute of Geochemistry, Institutions of Earth Science, Chinese Academy of Sciences, Wushan, Guangzhou 510640, China.
E-mail address: yuanpeng@gig.ac.cn (P. Yuan).

https://doi.org/10.1016/j.clay.2021.106019
Received 7 October 2020; Received in revised form 3 February 2021; Accepted 5 February 2021
Available online 2 March 2021

molecules (SAP gel). The [PO_4] balances the negative charge of [AlO_4] without the involvement of extra cations. The main component formed by acid-activated geopolymerization is amorphous aluminum phosphate hydrate ($AlPO_4{\cdot}nH_2O$). In $AlPO_4{\cdot}nH_2O$, aluminum exists as an aluminum-oxygen octahedron ([AlO_6]), which is the most stable coordination structure (Louati et al., 2016a). Thus, the resulting SAP geopolymers (Wagh, 2005) have excellent properties such as corrosion resistance (Wagh, 2011), efflorescence resistance (Wang et al., 2019a), thermal stability (Celerier et al., 2018) and dielectric property (Liu et al., 2010; Douiri et al., 2014). Moreover, Wagh (2004) assessed the energy usage during the phosphate binder production. The energy consumption of phosphate binder production was one-quarter that of Portland cement production, and the phosphorus in the spent SAP could be extracted and used as fertilizers for crops (Jelinski et al., 1992; Raven and Loeppert, 1996). In this regard, being phosphate-containing materials, SAP geopolymers are more sustainable and more environmentally friendly than AAS geopolymers.

Clay minerals reserves are abundant worldwide (Deng et al., 2017). Clay minerals are one of the major aluminosilicate sources for geopolymers preparation. Among the minerals, metakaolin (MK), the calcination product of kaolinite, is commonly used to prepare geopolymers because of its outstanding pozzolanic properties (Sabir et al., 2001; Wang et al., 2015; Toniolo and Boccaccini, 2017; Li et al., 2019; Zhang et al., 2020b). In recent years, with the growing concern on pollution control and clean production, the use of industrial solid waste as the raw materials of geopolymers has received increasing attention globally. Several solid wastes containing reactive silica and alumina, such as fly ash (FA) (Hajimohammadi et al., 2019), granulated blast-furnace slag (Komnitsas and Zaharaki, 2009; Khan et al., 2016), biomass ash (Alonso et al., 2019) and red mud (Afolabi et al., 2019), have been found as good candidate raw materials for AAS geopolymerization. However, the use of solid waste to prepare SAP geopolymers has rarely been studied, which limits the practical use of SAP geopolymers in the field of recycling of solid waste.

Fly ash is a commonly used solid waste for the preparation of AAS geopolymers. It is an abundant, readily available, and low-cost aluminosilicate source (Vassilev and Vassileva, 2005; Yao et al., 2015; Yan et al., 2016). Numerous studies have confirmed the advantages of FA for the preparation of AAS geopolymers; for example, it reduces the water requirement and increases the compressive strength of the geopolymers (Laskar and Talukdar, 2008; Provis et al., 2010; Zhang et al., 2014). Fly ash has been identified as one of the most suitable solid wastes for the preparation of AAS geopolymers. However, the feasibility of using FA for the preparation of SAP geopolymers remains unclear to date and the influence of FA on the properties of SAP geopolymers deserves investigation.

In this work, we used FA and MK to prepare SAP geopolymers and investigated the effects of the FA and MK amounts on the geopolymers composition, microstructure, and properties. The possible physical and chemical interactions of FA and MK during geopolymerization were explored based on comprehensive microscopic and spectroscopic characterizations of the reaction products.

2. Materials and methods

2.1. Materials

2.1.1. Precursors and acid activator

Fly ash (FA) was supplied by a thermal power plant in Foshan, Guangdong. The chemical compositions of FA are presented in Table 1. The calcium (Ca) content in FA was close to 10 mass%, which classifies FA as Class F (ASTM C618-19, 2019). The aluminum (Al) content of the FA was low, only 21.7 mass%. The loss on ignition (LOI) being almost zero indicates the low content of unburned organic matters such as carbon particles, which increases the water requirement (Zhang et al., 2016).

Metakaolin (MK) was obtained from the calcination of kaolinite (Maomin, Guangdong) in a muffle furnace at 750°C for 2 h. The main chemical compositions of kaolinite are presented in Table 1.

The acid activator was a phosphoric acid (85 mass%) solution.

2.1.2. Properties of the raw materials

The particle size distribution, specific surface area, and specific gravity of the FA and MK are listed in Table 2 and Fig. 1a. The results show that the MK particles were much larger than the FA particles, which was caused by the calcination treatment. The approximate specific gravities of the FA and MK are beneficial to mixing uniformity.

Fig. 1b is the scanning electron microscopy (SEM) image of the FA. Cenospheres, plerospheres and solid particles with varying sizes can be observed. According to the energy-dispersive spectroscopy (EDS) analysis, the Si/Al molar ratio of FA was 1.07 ± 0.23, and the contents of Si and Al, with different shapes were not constant. The MK particles maintained a plate-like microstructure (Fig. 1c). They were stacked together to form large clusters, which increased the particle size, and the Si/Al molar ratio of MK was 0.83 ± 0.01 according to the EDS test.

Fig. 2a shows the Fourier-transform infrared (FT-IR) spectra of FA and MK. The bands in the regions 1000–1100 cm^{-1} are signed to the Si-O-T(Si, Al) asymmetric stretching vibration (Pimraksa et al., 2011; Singhal et al., 2017). In the FT-IR spectrum of FA, the typical doublet at 776 and 793 cm^{-1} corresponds to the Si-O-Si vibration of quartz (Criado et al., 2005; Rozek et al., 2018). The band at approximately 570 cm^{-1} is attributed to the symmetric stretching vibration of Si-O-Al of mullite (Criado et al., 2005; Liu et al., 2016). The sharp band at 3642 cm^{-1} corresponds to the vibration of T (Si, Al)-O-H, which was not found in the MK.

The mineral compositions of the FA and MK can be identified by the X-ray diffraction (XRD) patterns (Fig. 2b). The abilities of the raw materials to undergo geopolymerization mainly depend on the amorphous phase. The presence of the amorphous phase in both raw materials is indicated as a broad diffraction pattern. Different short-range orders resulted in diverse center positions of the broad diffraction pattern, which was at 26° (2θ) in FA and at 22° (2θ) in the MK. According to the area of the broad diffraction pattern, the amorphous phase amounts can be compared (Williams et al., 2011). The amorphous phase content was rather low in the FA but high in the MK, which indicates that the FA had a much lower reactivity than the MK. Moreover, the main crystal phases in MK were quartz and illite, while those in FA were quartz, mullite, anhydrite, and hematite.

Table 2
Physical properties of the FA and MK.

Materials	specific gravity	Specific surface area (m^2/cm^3)	Particle size distribution (μm)		
			D10	D50	D90
FA	2.36	8.16	0.29	1.16	3.34
MK	2.30	0.77	7.38	29.33	58.35

Table 1
Chemical compositions of the FA and kaolinite (mass %).

Components	SiO_2	Al_2O_3	CaO	Fe_2O_3	K_2O	Na_2O	MgO	TiO_2	Others	LOI
FA	53.63	21.71	10.80	7.96	1.42	1.21	1.17	0.86	0.76	0.33
Kaolinite	47.69	36.48	0.08	0.69	0.65	0.07	0.11	0.36	0.26	13.47

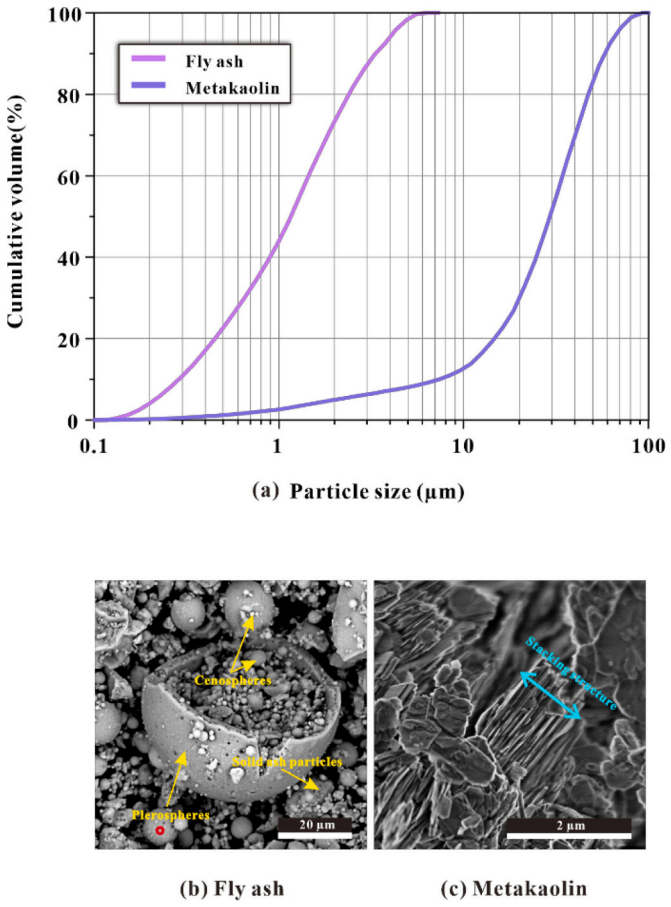

Fig. 1. (a) Particle size distribution of the FA and MK. SEM images of (b) FA and (c) MK.

2.2. Preparation of SAP geopolymers

The solid materials for synthesizing SAP geopolymers were the mixtures of MK and FA. Each of the solid mixtures was mixed by a ball mill for 1 h at 56 rmp to ensure uniformity. The acid activator was a mixture of phosphoric acid and ultrapure water. After the mixing, the solutions were cooled for 24 h before use.

Geopolymers were prepared by adding the solid mixture into acidic activator. The slurry was stirred by a cement mixer for 5 min. The resulting paste was cast into polytetrafluoroethylene (PTFE) molds (20 × 20 × 20 mm^3), which were then vibrated for 1 min to remove the air bubbles. The molds were covered with plastic wrap to prevent water loss. The specimens were cured at a temperature of 40°C and relative humidity (RH) of 90%. After six days, they were transferred to an oven, where they were dried at 80°C for 24 h without film. The final cubic specimens containing 100, 80, 70 and 50 mass% FA were designated as GFA, GFA_{80}, GFA_{70} and GFA_{50}, respectively. Then the specimens were aged at room temperature. All the samples were prepared by fixing the theoretical molar ratio of Al/P to one (Celerier et al., 2018; Gualtieri et al., 2015). The appropriate amount of water was added such that the groups of paste had similar fluidity. The details of the design are presented in Table 3.

2.3. Characterization methods

The contents of major elements were determined by X-ray fluorescence spectrometry (XRF) using wavelength-dispersive sequential scanning spectrometer (Shimadzu XRF-1800).

The particle size distribution and specific surface area were measured by JL-1177 laser particle size analyzer.

The setting times of fresh pastes were measured using the Vicat needle penetration tests according to the ASTM C191 standard (ASTM C191-19, 2019).

The compressive strength of SAP geopolymers on day 7 and day 100 was examined by cement compression machine, using a loading velocity of 0.5 N/s. In each group, at least seven specimens were tested. After the statistical testing to remove outliers, the remaining data were used for strength assessment.

The compressive strength results were analyzed using one-way analysis of variance (ANOVA). Tamhane's T2 ($P = 0.05$) was used for

Table 3
The mass fraction of FA in raw materials, the molar ratio and solid-to-liquid mass ratio (S/L) between raw material and phosphoric acid activator.

Samples	FA (mass%)	MK (mass%)	Al/P*	Si/Al*	S/L
GFA	100	0	1	2.15	1.27
GFA_{80}	80	20	1	1.78	1.19
GFA_{70}	70	30	1	1.62	1.16
GFA_{50}	50	50	1	1.34	1.09

* The mole ratios of Al/P and Si/Al was based on the XRF analyses and the mass ratios of FA and MK in solid mixtures. The total content of SiO_2 and Al_2O_3 were calculated as the mass of solid mixture was determined. The molar ratio of Al/P was kept to 1 by adjusting the mass of phosphoric acid.

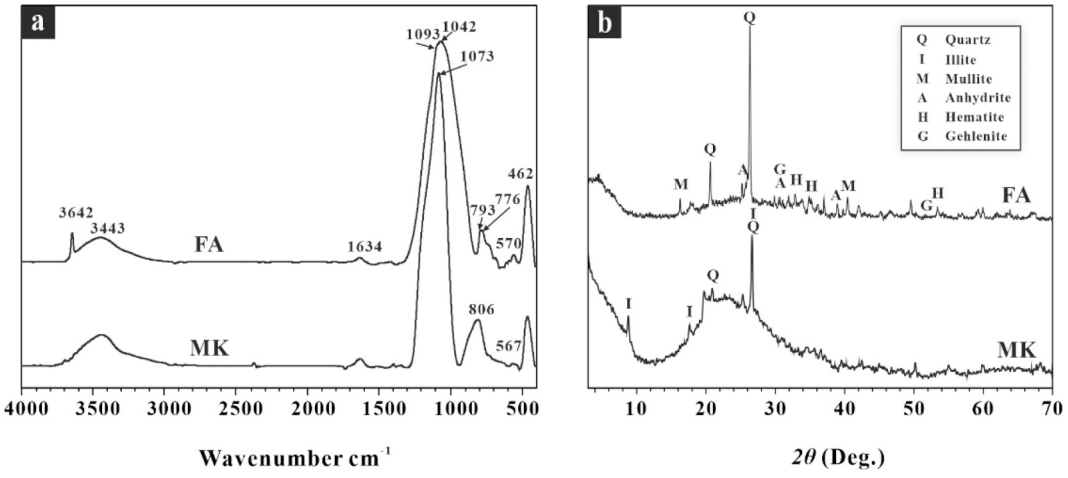

Fig. 2. (a) FT-IR spectra and (b) XRD patterns of the FA and MK (Quartz: JCPDS No. 46–1045, Illite: JCPDS No. 26–0911, Mullite: JCPDS No. 83–1881, Anhydrite: JCPDS No. 37–1496, Gehlenite: JCPDS No. 35–0755 and Hematite: JCPDS No. 33–0664).

post hoc multiple comparisons to determine the group differences.

X-ray diffraction (XRD) patterns were obtained using a Bruker D8 Advance diffractometer with Cu-Kα radiation at 40 kV and 40 mA; the scanning range was 3° to 70°, with a speed of 3°/min and a step width of 0.02°.

Fourier-transform infrared spectra (FT-IR) were obtained using a Bruker Vertex-70 FT-IR spectrometer. In the FT-IR testing, the powdery sample mixed with KBr was pressed into a transparent round slice and tested in the wavenumber range from 4000 cm^{-1} to 400 cm^{-1} under transmittance mode.

Thermal gravimetry with differential scanning calorimetry (TG-DSC) was applied to detect the thermal decomposition and phase transition of samples within the range of 30°C to 1000°C. The test was completed on a Netzsch STA 409 PC instrument with a heating rate of 10°C/min under an air atmosphere.

A field emission scanning electron microscope (FESEM, HITACHI SU8010) was used to observe the samples microstructure. Meanwhile, the equipped energy-dispersive spectrometer (EDS) was used to analyze the element type and micro-components content.

3. Results and discussion

3.1. Setting time

Fig. 3 shows the initial and final setting times of SAP geopolymers with different FA/MK ratios. The initial setting time corresponds to when the monomer concentrations reach the level for polycondensation to occur and the gel partially forms (Wang et al., 2018). For GFA, GFA_{80}, GFA_{70} and GFA_{50}, the initial setting time was 12, 20, 89 and 875 min, respectively. The increasing fraction of MK resulted in the initial setting time prolonging dramatically. Previous investigations indicate that divalent metal cations (e.g., Mg^{2+} and Ca^{2+}) effectively shorten the initial setting time (Wang et al., 2019b, 2020). For GFA, the short initial setting time was mainly caused by the Ca in the FA. Divalent metals oxides commonly have a higher solubility in an acid environment than trivalent metal cations (Wagh and Jeong, 2003). Thus, Ca was dissolved before Al to form calcium phosphate at the beginning of the SAP geopolymerization. The calcium phosphate combined with a large amount of H_2O, causing the specimen to rapidly solidify. In GFA_{80}, GFA_{70} and GFA_{50}, the MK partially substituted the FA, and the content of active Al gradually increased. When large amounts of Al were released after Ca dissolution, $[PO_4]$ began to react with $[AlO_4]$. Because the solubility of aluminum phosphate is much lower than that of calcium phosphate, the formation of Al-containing oligomers of SAP may cause calcium phosphate to redissolve. The setting times of GFA_{80}, GFA_{70} and GFA_{50} were affected by the further SAP polycondensation, which is a slow process (Dan et al., 2008). Hence, both the initial and final setting times multiplied with the increase in the MK amount in the raw materials. Nonetheless, compared with the MK-based SAP geopolymers (the final setting time was more than 48 h (Wang et al., 2018)), the SAP geopolymers with FA as the main raw materials had a lower setting time, which is more practical and energy-efficient.

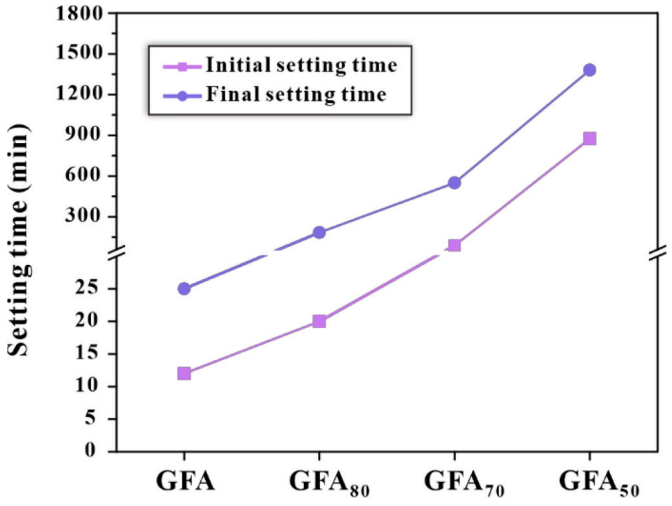

Fig. 3. Initial and final setting time of the SAP geopolymers with different contents of the MK.

3.2. Compressive strength

The compressive strengths of different SAP geopolymers on day 7 and day 100 are displayed in Fig. 4. The GFA strength on day 7 reached 8.6 MPa. After further aging at room temperature for 93 days, the compressive strength of GFA was reduced to 6.3 MPa. The strength of GFA_{80}, GFA_{70}, and GFA_{50} on day 7 were over 24.0 MPa, and GFA_{50} had the highest compressive strength (43.5 MPa) on day 100. The one-way ANOVA analysis results (Table 4) showed significant differences ($P < 0.05$) among the groups of geopolymers with different mass fractions of MK; the MK content affected both the day-7 and day-100 compressive strengths of the SAP geopolymers. The post hoc multiple comparisons confirmed the degree of this influence. Different lowercase letters (i.e., a, b, and c) after values in the same rows of Table 4 represent significant differences at $P = 0.05$. The results indicate that adding 20 and 30 mass % MK had a similar effect on compressive strength. The addition of 50 mass% MK had the greatest impact, which greatly increased the compressive strength of GFA_{50}. For the compressive strength increment in 7–100 days, the post hoc multiple comparisons showed that only the addition of 50 mass% MK enhanced the compressive strength increment. No difference in increment existed between GFA, GFA_{80}, and GFA_{70}. The MK mass fraction lower than 50 mass% cannot contribute to the sustained growth, which proves that the day-7 compressive strengths of GFA, GFA_{80}, and GFA_{70} represented the final mechanical performance.

The calcium phosphate gel only displayed fast polycondensation but had no capacity of developing compressive strength (Gualtieri et al., 2015; Tchakouté et al., 2017; Wang et al., 2019b; Wang et al., 2020). Increasing the mass fraction of MK to enrich the active Al leads to both excellent short- and long-term compressive strengths. The GFA_{80} sample

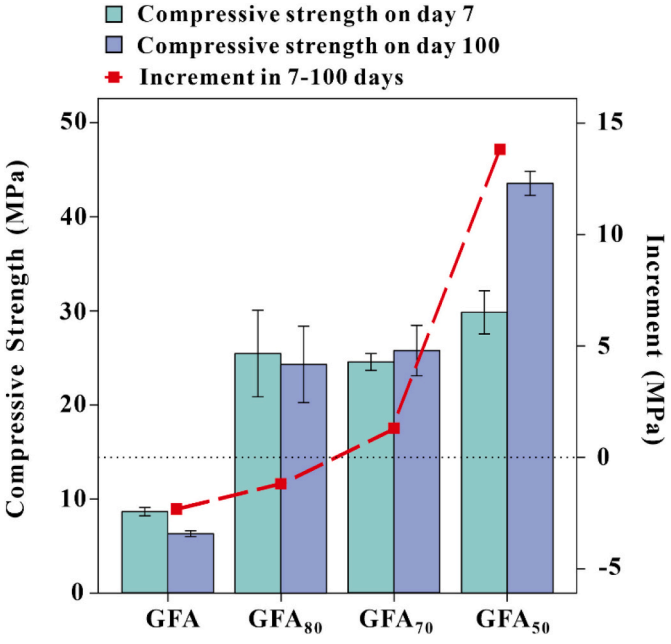

Fig. 4. Compressive strengths of the SAP geopolymers with the different mass fractions of FA and MK on day 7 and day 100, and the increment of compressive strength in 7–100 days. (error bar represents the 95% confidence interval).

Table 4
Compressive strengths on day 7 and day 100 and the increment of compressive strength in 7–100 days of the SAP geopolymers with different mass fractions of FA and MK. The ANOVA test and Tamhane's T2 test showing the mean differences.

	Compressive strength (MPa)				ANOVA	
	GFA	GFA_{80}	GFA_{70}	GFA_{50}	F	P
Day 7	8.6a	25.5bc	24.5b	29.8c	233.15	0.00
Day 100	6.3a	24.3b	25.7b	43.5c	675.62	0.00
Increment	−2.3a	−1.2a	1.2a	13.7b	103.23	0.00

a, b, c Means with the same lowercase letter in the same rows are not statistically different (P = 0.05).

had only 20 mass% MK but featured an acceptable proper setting time and compressive strength on day 100 (ASTM C150/C150M-20, 2020).

3.3. Changes in the compositions of SAP geopolymers

3.3.1. XRD analysis

The mineralogical compositions of SAP geopolymers are illustrated in Fig. 5a. The central positions of the broad diffraction pattern in all geopolymers are approximately 27° (2θ) without displacement comparing with FA (Fig. 2b), but the area of the broad diffraction pattern is significantly larger than that of FA, which indicates the formation of an amorphous phase. This result conforms to the SAP geopolymerization in previous studies in which products with a broad diffraction pattern centered at 27° (2θ) were proved to be amorphous berlinite ($AlPO_4$) (Louati et al., 2016a). Furthermore, $AlPO_4$ is the isostructure of quartz, and its XRD patterns are similar to those shown in Fig. 5b. Amorphous $AlPO_4$ features the same short-range order with quartz, as well as properties such as hardness and thermal stability. Silico-aluminophosphate geopolymers containing abundant amorphous $AlPO_4$ feature excellent mechanical properties.

In GFA, the characteristic diffraction of anhydrite ($CaSO_4$) in FA (Fig. 2b) was absent, which indicates that the crystal structures of $CaSO_4$ were destroyed under the action of the acid-activator. In GFA_{80}, GFA_{70}, and GFA_{50}, the Ca released from $CaSO_4$ existed mainly in the form of brushite ($CaHPO_4{\cdot}2H_2O$) whose diffractions are shown in Fig. 5a. However, no diffraction of $CaHPO_4{\cdot}2H_2O$ crystal was found in GFA. Perhaps, Ca occurred in GFA only as amorphous calcium phosphate (ACP), which exhibits the increasing broad diffraction pattern area, even the amount of active Al in FA was low. Amorphous calcium phosphate is an inevitable intermediate product when Ca reacts with $[PO_4]$ (Tao et al., 2007), which will transform into other stable calcium phosphate phases (Brown, 1962). Moreover, the other crystalline phases including quartz, hematite, gehlenite, and mullite in the raw materials did not participate in the SAP geopolymerization and remained in the final products.

3.3.2. FT-IR analysis

The spectra of GFA, GFA_{80}, GFA_{70}, and GFA_{50} are presented in Fig. 6a–d. The vibration bands around 3225 cm^{-1}, 918 cm^{-1}, and 549 cm^{-1} in the geopolymers correspond to aluminum phosphate hydrate ($AlPO_4{\cdot}nH_2O$) (Fig. 6e) (Boonchom and Kongtaweelert, 2009). Based on the XRD analysis (Fig. 5a), which indicated that the SAP geopolymerization product is amorphous phases, and the FT-IR analysis, the major product of SAP geopolymerization was identified as amorphous $AlPO_4{\cdot}nH_2O$. However, it was hard to distinguish the Al-O-P vibration around 1100 cm^{-1} because it was overlapped by the asymmetric stretching vibration of Si—O which was located at almost the same position (Sitarz, 2008; Zhang et al., 2020c). The O—H vibration peak is a representative peak to demonstrate the existence of amorphous $AlPO_4{\cdot}nH_2O$. In the SAP geopolymers, in addition to the common O—H stretching vibration of absorbed H_2O (3434 cm^{-1} and 1643 cm^{-1}), a new O—H vibration band occurred at 3225 cm^{-1} which is assigned to the crystal water in $AlPO_4{\cdot}nH_2O$. Different from the case of GFA, the peak intensity of 3225 cm^{-1} was enhanced when the content of MK was increased from 20 to 50 mass%, which was the result of the increased $AlPO_4{\cdot}nH_2O$ amount.

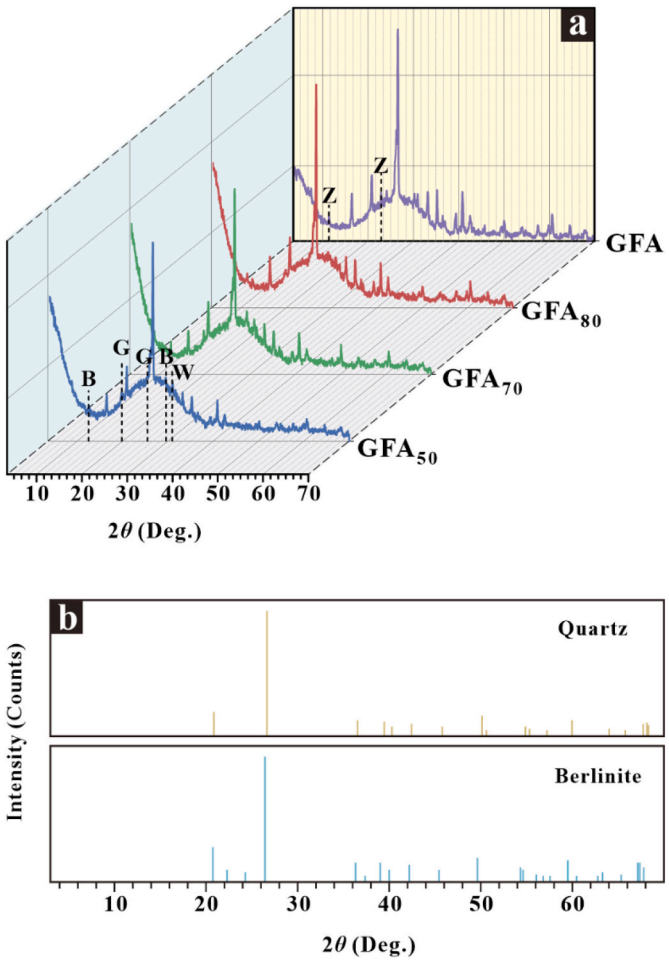

Fig. 5. (a) XRD spectra of the GFA, GFA_{80}, GFA_{70}, and GFA_{50} (B: brushite, JCPDS No. 72–1240, G: grossite, JCPDS No. 23–1037, W: whitlockite, JCPDS No. 09–0169 and Z: zeolite, JCPDS No. 31–0580). (b) XRD standard spectra of the quartz and berlinite (JCPDS No. 10–0423).

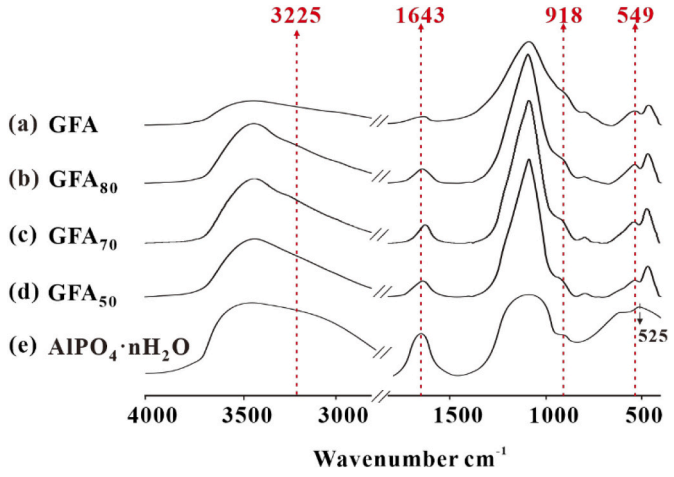

Fig. 6. FT-IR spectra of the (a) GFA, (b) GFA_{80}, (c) GFA_{70}, (d) GFA_{50}, and (e) $AlPO_4{\cdot}nH_2O$. The red dotted line indicates the characteristic vibration peaks of SAP geopolymers.

The vibration bands at 549 cm^{-1} did not match the P-O-Al vibration (525 cm^{-1}) in the pure $AlPO_4{\cdot}nH_2O$ and overlapped with the Si-O-Al stretching vibration of mullite (570 cm^{-1}), which did not participate in the SAP geopolymerization. The blueshift of P-O-Al vibration was caused by the partial replacement of [PO_4] by [SiO_4] around the Al atom (Louati et al., 2016b). This indicates that one [AlO_4] monomer can undergo polycondensation with [PO_4] and [SiO_4] at the same time. The formed Si-O-Al-O-P is one of the structural units of SAP geopolymers. Moreover, the vibration band at 918 cm^{-1} is assigned to the T(Al, P)-OH vibration (Louati et al., 2016b; Zhang et al., 2020a). With the increasing mass fraction of FA in the raw materials, the SAP geopolymers exhibited a significant strengthening of this band, which represents an increase in the unreacted T(Al, P)-OH amount in the resulting geopolymers.

3.3.3. TG-DSC analysis

The experimental results of TG curves for each group of SAP geopolymers are presented in Fig. 7a. The GFA_{50} sample featured the largest total weight loss (20.6%) between 30°C and 1000°C, followed by GFA_{70} (17.6%) and then GFA_{80} (16.3%). While GFA only lost 9.0% of its weight. Most of the weight loss occurred before 240°C, which conforms to the characteristics of crystal water. Moreover, the weakening trend of weight loss was consistent with the decreasing amount of O—H assigned to the $AlPO_4{\cdot}nH_2O$, which has been proved by FT-IR analysis (Fig. 6).

The differential scanning calorimetry (DSC) curves (Fig. 7b) reflect the SAP geopolymers thermodynamic stability. The only exothermic peak appearing around 650°C corresponds to the phase transformation of monetite ($CaHPO_4$) which was formed from brushite ($CaHPO_4{\cdot}2H_2O$) losing the crystal water at 200°C. The $CaHPO_4$ further dehydrated to be calcium pyrophosphate ($Ca_2P_2O_7$) when the temperature increased to 650°C (Wikholm et al., 1975). The phase transformation of $CaHPO_4$ at high temperatures causes the poor thermodynamic stability of GFA_{80}, GFA_{70}, and GFA_{50}. For the dehydrated amorphous $AlPO_4$, it was stable even the temperature up to 1000°C (Youssif et al., 2004), which results in the SAP geopolymers exhibiting excellent thermodynamic stability (Wagh, 2011).

3.4. Changes in the microstructure of SAP geopolymers

The SEM images of GFA aged for 7 and 100 days are displayed in Fig. 8a and b. The particle surface was covered by a gelatinous substance on day 7 (Fig. 8a). Through EDS analysis, the main elements in the microstructure were P, Ca, Al, and Si (Fig. 8c). However, the gelatinous substance disappeared after 100 days accompanied by the formation of the needle- and slice-like particles (Fig. 8b). Needles were distributed over the matrix surface; cracks and a few slices were interspersed among the needles (Fig. 8d). The whole matrix was analyzed via EDS to obtain the elemental map. As shown in Fig. 8e, Ca and P were spread all over the matrix at the highest concentrations, followed by Al and Si. The evolution of the Ca-rich microstructure is attributed to the ACP which is an unstable intermediate. Under the different conditions (e.g., temperature, pH, and Ca/P molar ratio), ACP could transform into the thermodynamically stable $CaHPO_4{\cdot}2H_2O$, $CaHPO_4$, or hydroxyapatite (Tao et al., 2007) in the shape of slices (Fernández et al., 1998), needles (Kumar et al., 2004), or spheres (Kumar et al., 2004). Most of the needle-like calcium phosphates observed in GFA were nanoscale. Those nanorods were difficult to be detected by XRD in the form of crystal patterns but featured the amorphous diffraction pattern (Onuma et al., 2000). The reason why there are abundant nanorods of calcium phosphate in GFA can be attributed to the presence of excess phosphoric acid. Although the dosage of acid activator was calculated to match the theoretical content of Al in the raw materials, the percentage of active Al was low in FA. Most of the phosphoric acid reacted with Ca to form ACP during the geopolymerization. The transformation of ACP into needle-like particles loosened the original structure of GFA. Hence, the compressive strength of GFA was reduced after aging for 100 days (Fig. 4).

Fig. 9a is the SEM image of GFA_{80} after day-100 aging. The GFA_{80} appeared as a compact solid with some cracks. Different from GFA, the GFA_{80} hardly featured nanorods and slices of calcium phosphate, which means that the calcium phosphate particles in GFA_{80} did not rearrange. The Ca distribution in GFA_{80} was obtained by EDS mapping analysis. In Fig. 9d, green spots represent evenly distributed Ca with low density. The matrix was rich in Al and P, which had the same distribution patterns. This reflects that calcium phosphate was dispersed among the SAP. According to the XRD and TG-DSC analyses, MK resulted in the species of the formed calcium phosphate different from that in GFA. Some parts of Ca formed $CaHPO_4{\cdot}2H_2O$ particles, which were deposited in the SAP gel. The others consisting of the ACP was immobilized by SAP at the initial stage of the reaction, which prevented ACP from transforming to nanorods.

Some areas in Fig. 9d exhibit high concentration of Al and P is contributed to the SAP formed by geopolymerization. The Si-rich parts were due to the unreacted particles (e.g., cenospheres, quartz, and MK). Fig. 9b is the local enlarged image of the SAP and unreacted cenospheres. A mass of pores is observed in the region containing SAP. The porosity was probably caused by the evaporation of water (Dan et al., 2008; Tchakouté et al., 2017). As depicted in Fig. 9b, SAP adhered to the cenospheres surface and cements them to the other particles, which might be due to the abundant Si-OH groups on the surface of cenospheres that facilitated the polycondensation (Stumm and Morgan, 2012). For MK, the tetrahedral SiO_4 sheet can reobtain –OH after its exposure to acidic medium (Henri, 1996). The SAP gel formed on the surface of the tetrahedral SiO_4 sheet and cemented multiple sheets together. This phenomenon can be reflected by the element distribution

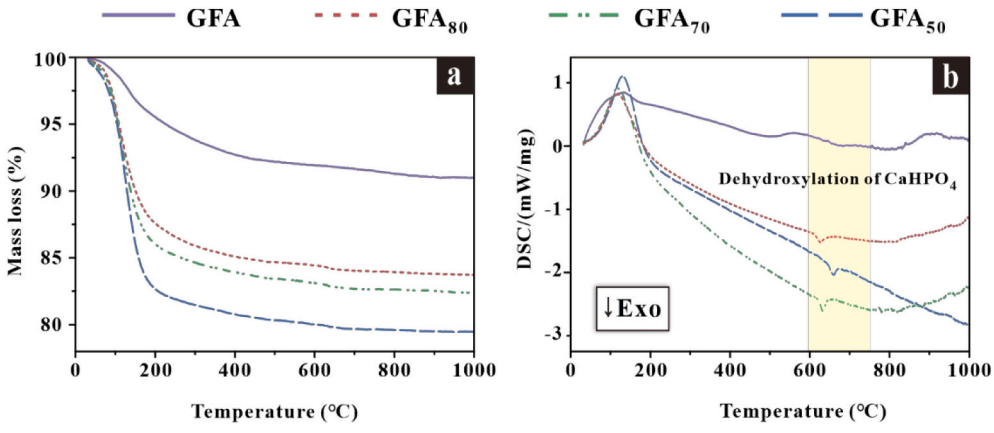

Fig. 7. (a) TG and (b) DSC curves of GFA, GFA_{80}, GFA_{70}, and GFA_{50}.

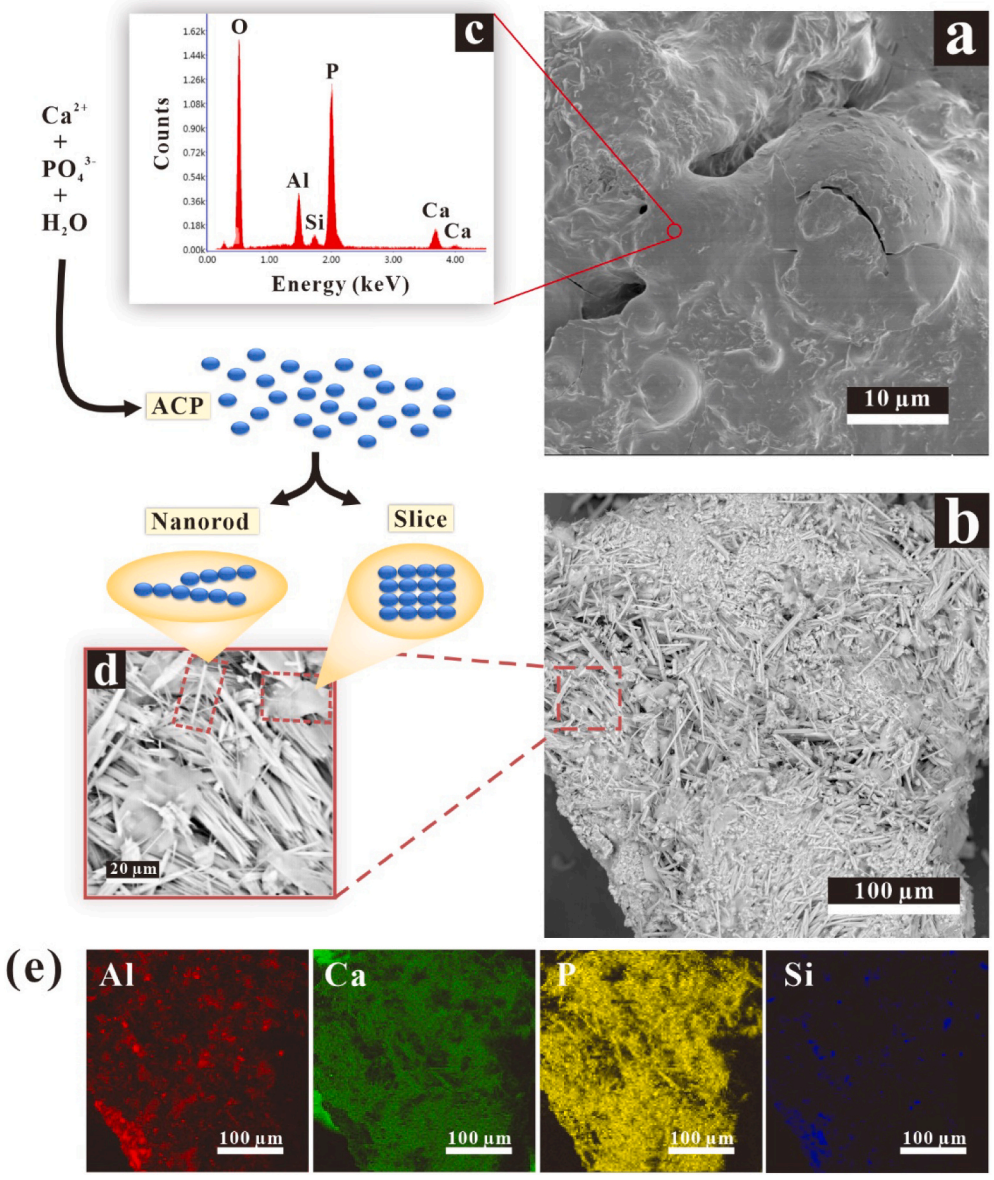

Fig. 8. SEM images of GFA (a) on day 7 and (b) on day 100. (c) EDS spot analysis of the GFA matrix. (d) local enlarged image of the nanorod and slice in the GFA. (e) corresponding quantitative EDS maps for Ca, P, Al, and Si.

of plate-like particles shown in Fig. 9c, which shows a high concentration of Si and relatively low concentrations of Al and P.

3.5. Mechanism of SAP geopolymerization with the different mass fractions of FA and MK

The above analyses of the SAP geopolymers show that the different mass fractions of FA and MK in the raw materials affected geopolymerization resulting from the different contents of Ca and active Al. At the beginning of the geopolymerization, Ca was released from FA before Al, which was caused by the higher solubility of calcium oxide than aluminum oxide under acidic conditions. Abundant Ca reacted with phosphoric acid and water to form ACP particles. This quick-reaction shortened the initial setting time of geopolymers. As Al was released in the later stage of geopolymerization, the phosphoric acid preferably combined with [AlO_4] monomers because aluminum phosphate has a lower solubility than calcium phosphate. Therefore, the ACP particles re-dissolved to release [PO_4] monomers and react with [AlO_4] monomers if the amounts of [PO_4] monomers are insufficient to react with Ca and Al simultaneously. For GFA, owing to the lack of active Al, the ACP did not re-dissolve so that abundant ACP transformed to the needle- and slice-like particles that damaged the structure tightness of GFA in the later stage.

For the geopolymerization with a high mass fraction of MK, adequately active Al was released from MK to form SAP gel. Under the effect of Si-OH groups which exists in the FA or is newly formed on the residual tetrahedral SiO_4, the SAP tended to form on the surface of these particles and bonded them together to form a compact matrix. Although the SAP gel porosity was caused by the evaporation of water, as the main coordinate of Al in SAP gel, [AlO_6] linking with [PO_4] provided a stable isostructure of quartz. Thus, the SAP geopolymers showed excellent compressive strength. However, the polycondensation of SAP gel was a slow process, and the setting time was inevitably prolonged.

4. Conclusions

Metakaolin and fly ash with different ratios were used as aluminosilicate sources to synthesize silico-aluminophosphate (SAP)

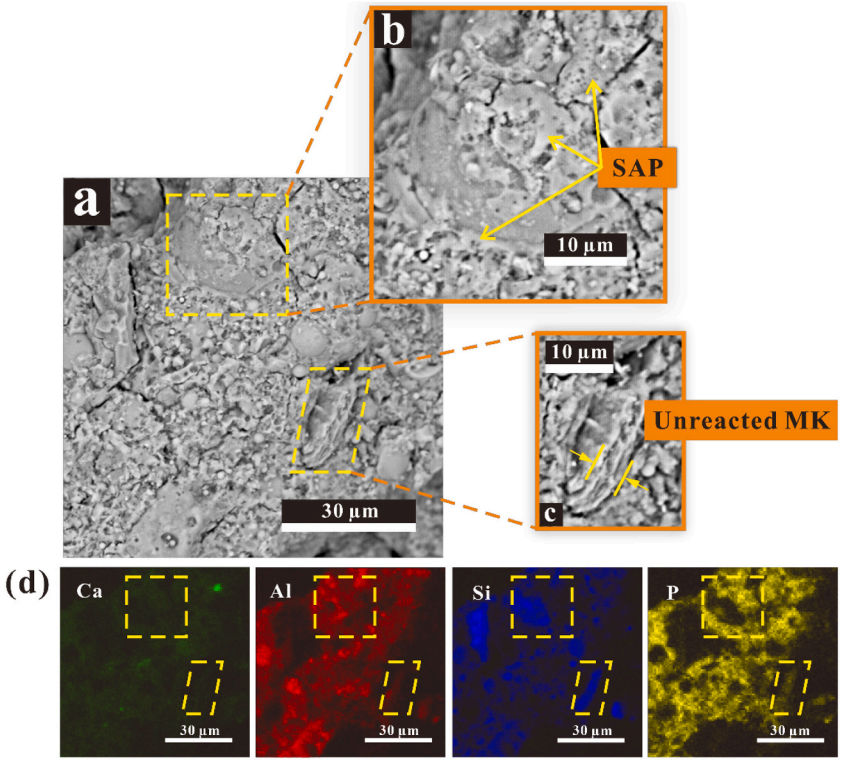

Fig. 9. (a) SEM image of GFA_{80} after day-100 aging. Local enlarged images of (b) porous SAP and (c) unreacted MK bonded by SAP. (d) the corresponding quantitative EDS maps for Ca, Al, Si, and P.

geopolymers. A high mass fraction of fly ash in the raw materials was used for the SAP geopolymers preparation. The resulting SAP geopolymers exhibited excellent properties including short setting time and high compressive strength. These properties were dramatically affected by the relative ratios of fly ash and metakaolin. The high fly ash content provided abundant calcium, which shortened the setting time but deteriorated the compressive strength by forming amorphous calcium phosphate. With the increasing metakaolin content, the SAP gel formation was enhanced, which improved the compressive strength by inhibiting the destructive effect of amorphous calcium phosphate on the geopolymers microstructure. However, a high metakaolin content resulted in prolonged setting time, due to the slow polycondensation of SAP gel. These results demonstrate that the SAP geopolymers preparation using metakaolin and solid waste, that is, fly ash, is feasible; moreover, the major properties of SAP geopolymers can be adjusted by regulating the relative ratios of fly ash and metakaolin, allowing for versatile applications.

Declaration of Competing Interest

The authors declare that they have no known competing financial interests or personal relationships that could have appeared to influence the work reported in this paper.

Acknowledgments

This work was financially supported by the National Special Support for High-Level Personnel and the National Natural Science Foundation of China (Grant No. 41972045). This is a contribution (No. IS-2984) from GIGCAS.

References

Wang, K.-T., He, Y., Song, X.-L., Cui, X.-M., 2015. Effects of the metakaolin-based geopolymer on high-temperature performances of geopolymer/PVC composite materials. Appl. Clay Sci. 114, 586–592. https://doi.org/10.1016/j.clay.2015.07.008.

ASTM C191-19, 2019. Standard Test Methods for Time of Setting of Hydraulic Cement by Vicat Needle. ASTM International, West Conshohocken, PA. https://doi.org/10.1520/C0191-19.

ASTM C618-19, 2019. Standard Specification For Coal Fly Ash and Raw or Calcined Natural Pozzolan For Use In Concrete. ASTM International, West Conshohocken, PA. https://doi.org/10.1520/C0618-19.

Abdullah, M.A.B., Ariffin, N., Abdullah, M.M.A.B., Mohd Arif Zainol, M.R.R., Murshed, M.F., Hariz, Z., Faris, M.A., Bayuaji, R., Abd Rahim, S.Z., Muhammad Suandi, M.E., Mat Saad, M.N., Ghazali, M.F., 2017. Review on Adsorption of Heavy Metal in Wastewater by using Geopolymer. MATEC Web of Conferences 97. https://doi.org/10.1051/matecconf/20179701023.

Afolabi, L.O., Ariff, Z.M., Megat-Yusoff, P.S.M., Al-Kayiem, H.H., Arogundade, A.I., Afolabi-Owolabi, O.T., 2019. Red-mud geopolymer composite encapsulated phase change material for thermal comfort in built-sector. Sol. Energy 181, 464–474. https://doi.org/10.1016/j.solener.2019.02.029.

Alonso, M.M., Gascó, C., Morales, M.M., Suarez, J.A., Puertas, F., 2019. Olive biomass ash as an alternative activator in geopolymer formation: a study of strength, durability, radiology and leaching. Cem. Concr. Compos. 104, 103384. https://doi.org/10.1016/j.cemconcomp.2019.103384.

ASTM C150/C150M-20, 2020. Standard Specification for Portland Cement. ASTM International, West Conshohocken, PA. https://doi.org/10.1520/C0150_C0150M-20.

Bakharev, T., 2005. Resistance of geopolymer materials to acid attack. Cem. Concr. Res. 35, 658–670. https://doi.org/10.1016/j.cemconres.2004.06.005.

Bernal, S.A., Deventer, J.S.J.V., Provis, J.L., 2015. What Happens to 5 Year Old Metakaolin Geopolymers' the Effect of Alkali Cation, 1st International Conference on Calcined Clays for Sustainable Concrete. https://doi.org/10.1007/978-94-017-9939-3_39.

Boonchom, B., Kongtaweelert, S., 2009. Study of kinetics and thermodynamics of the dehydration reaction of $AlPO_4 \cdot H_2O$. J. Therm. Anal. Calorim. 99, 531–538. https://doi.org/10.1007/s10973-009-0113-5.

Brown, W.E., 1962. Octacalcium phosphate and hydroxyapatite. Nature 196, 1048. https://doi.org/10.1038/1961048b0.

Celerier, H., Jouin, J., Mathivet, V., Tessier-Doyen, N., Rossignol, S., 2018. Composition and properties of phosphoric acid-based geopolymers. J. Non-Cryst. Solids 493, 94–98. https://doi.org/10.1016/j.jnoncrysol.2018.04.044.

Criado, M., Palomo, A., Fernandezjimenez, A., 2005. Alkali activation of fly ashes. Part 1: effect of curing conditions on the carbonation of the reaction products. Fuel 84, 2048–2054. https://doi.org/10.1016/j.fuel.2005.03.030.

Dan, S.P., Hanna, J.V., Davis, J., Blackford, M.G., Latella, B.A., Sasaki, Y., Vance, E.R., 2008. Relative strengths of phosphoric acid-reacted and alkali-reacted metakaolin materials. J. Mater. Sci. 43, 6562–6566. https://doi.org/10.1007/s10853-008-2913-6.

Davidovits, J., 1991. Geopolymers: inorganic polymeric new materials. J. Therm. Anal. Calorim. 37 (8), 1633–1656. https://doi.org/10.1007/BF01912193.

Davidovits, J., 2017. Geopolymers: Ceramic-like inorganic polymers. J. Ceram. Sci. Technol. 8, 335–350. https://doi.org/10.4416/JCST2017-00038.

Deng, L.L., Yuan, P., Liu, D., Annabi-Bergaya, F., Zhou, J.M., Chen, F.R., Liu, Z.W., 2017. Effects of microstructure of clay minerals, montmorillonite, kaolinite and halloysite, on their benzene adsorption behaviors. Appl. Clay Sci. 143, 184–191. https://doi.org/10.1016/j.clay.2017.03.035.

Douiri, H., Louati, S., Baklouti, S., Arous, M., Fakhfakh, Z., 2014. Structural, thermal and dielectric properties of phosphoric acid-based geopolymers with different amounts of H_3PO_4. Mater. Lett. 116, 9–12. https://doi.org/10.1016/j.matlet.2013.10.075.

Duxson, P., Fernández-Jiménez, A., Provis, J.L., Lukey, G.C., Palomo, A., Deventer, J.S.J. V., 2007. Geopolymer technology: the current state of the art. J. Mater. Sci. 42, 2917–2933. https://doi.org/10.1007/s10853-006-0637-z.

Fernández, E., Gil, F.J., Best, S.M., Ginebra, M.P., Driessens, F.C.M., Planell, J.A., 1998. Improvement of the mechanical properties of new calcium phosphate bone cements in the $CaHPO_4$-$Ca_3(PO_4)_2$ system: compressive strength and microstructural development. J. Biomed. Mater. Res. https://doi.org/10.1002/(SICI)1097-4636(19980915)41:4<560::AID-JBM7>3.0.CO;2-A.

Font, A., Borrachero, M., Soriano, L., Monzo, J., Romero, A., Payá, J., 2018. New eco-cellular concretes: Sustainable and energy-efficient materials. Green Chem. 20 https://doi.org/10.1039/c8gc02066c.

Gualtieri, M.L., Romagnoli, M., Gualtieri, A.F., 2015. Preparation of phosphoric acid-based geopolymer foams using limestone as pore forming agent - thermal properties by in situ XRPD and Rietveld refinements. J. Eur. Ceram. Soc. 35, 3167–3178. https://doi.org/10.1016/j.jeurceramsoc.2015.04.030.

Hajimohammadi, A., Tuan, N., Vongsvivut, J., 2019. Interfacial chemistry of a fly ash geopolymer and aggregates. J. Clean. Prod. 231, 980–989. https://doi.org/10.1016/j.jclepro.2019.05.249.

Henri, Roques, 1996. Chemical water treatment: principles and practice. VCH, New York, N. Y, pp. 1–620 (ISBN 1-56081-518-3).

van Jaarsveld, J.G.S., van Deventer, J.S.J., 1999. Effect of the alkali metal activator on the properties of fly ash-based geopolymers. Ind. Eng. Chem. Res. 38, 3932–3941. https://doi.org/10.1021/ie980804b.

Jelinski, L.W., Graedel, T.E., Laudise, R.A., McCall, D.W., Patel, C.K.N., 1992. Industrial ecology-concepts and approaches. Proc. Natl. Acad. Sci. U. S. A. 89, 793–797. https://doi.org/10.1073/pnas.89.3.793.

Joussein, E., Soubrand, M., Pascaud, G., Cogulet, A., Rossignol, S., 2019. Immobilization of Pb from mine sediments in metakaolin-based geomaterials. Environ. Sci. Pollut. Res. https://doi.org/10.1007/s11356-019-04737-7.

Khan, M.S.H., Castel, A., Akbarnezhad, A., Foster, S.J., Smith, M., 2016. Utilisation of steel furnace slag coarse aggregate in a low calcium fly ash geopolymer concrete. Cem. Concr. Res. 89, 220–229. https://doi.org/10.1016/j.cemconres.2016.09.001.

Komnitsas, K., Zaharaki, D., 2009. Utilisation of Low-Calcium Slags to Improve the Strength and Durability of Geopolymers. https://doi.org/10.1533/9781845696382.2.343.

Kumar, R., Prakash, K.H., Cheang, P., Khor, K.A., 2004. Temperature Driven Morphological changes of Chemically Precipitated Hydroxyapatite Nanoparticles. Langmuir the Acs Journal of Surfaces & Colloids 20, 5196–5200. https://doi.org/10.1021/la049304f.

Laskar, A.I., Talukdar, S., 2008. Rheological behavior of high performance concrete with mineral admixtures and their blending. Constr. Build. Mater. 22, 2345–2354. https://doi.org/10.1016/j.conbuildmat.2007.10.004.

Li, Z., Zhang, S., Zuo, Y., Chen, W., Ye, G., 2019. Chemical deformation of metakaolin based geopolymer. Cem. Concr. Res. 120, 108–118. https://doi.org/10.1016/j.cemconres.2019.03.017.

Liu, L.P., Cui, X.M., He, Y., Yu, J.L., 2010. Study on the dielectric properties of phosphoric acid-based geopolymers. Mater. Sci. Forum 663-665, 538–541. https://doi.org/10.4028/www.scientific.net/MSF.663-665.538.

Liu, Y., Yan, C., Zhang, Z., Wang, H., Zhou, S., Zhou, W., 2016. A comparative study on fly ash, geopolymer and faujasite block for Pb removal from aqueous solution. Fuel 185, 181–189. https://doi.org/10.1016/j.fuel.2016.07.116.

Louati, S., Baklouti, S., Samet, B., 2016a. Acid based geopolymerization kinetics: effect of clay particle size. Appl. Clay Sci. 132-133, 571–578. https://doi.org/10.1016/j.clay.2016.08.007.

Louati, S., Baklouti, S., Samet, B., 2016b. Geopolymers based on phosphoric acid and illito-kaolinitic clay. Adv. Mater. Sci. Eng. 2016, 1–7. https://doi.org/10.1155/2016/2359759.

Mathivet, V., Jouin, J., Gharzouni, A., Sobrados, I., Celerier, H., Rossignol, S., Parlier, M., 2019. Acid-based geopolymers: Understanding of the structural evolutions during consolidation and after thermal treatments. J. Non-Cryst. Solids 512, 90–97. https://doi.org/10.1016/j.jnoncrysol.2019.02.025.

Onuma, K., Oyane, A., Tsutsui, K., Tanaka, K., Treboux, G., Kanzaki, N., Ito, A., 2000. Precipitation kinetics of hydroxyapatite revealed by the continuous-angle laser light-scattering technique. J. Phys. Chem. B 104, 10563–10568. https://doi.org/10.1021/jp002697g.

Pimraksa, K., Chindaprasirt, P., Rungchet, A., Sagoe-Crentsil, K., Sato, T., 2011. Lightweight geopolymer made of highly porous siliceous materials with various Na_2O/Al_2O_3 and SiO_2/Al_2O_3 ratios. Mater. Sci. Eng. A 528, 6616–6623. https://doi.org/10.1016/j.msea.2011.04.044.

Provis, J.L., Duxson, P., van Deventer, J.S.J., 2010. The role of particle technology in developing sustainable construction materials. Adv. Powder Technol. 21, 2–7. https://doi.org/10.1016/j.apt.2009.10.006.

Raven, K.P., Loeppert, R.H., 1996. Microwave digestion of fertilizers and soil amendments. Commun. Soil Sci. Plant Anal. 27, 2947–2971. https://doi.org/10.1080/00103629609369754.

Rozek, P., Krol, M., Mozgawa, W., 2018. Spectroscopic studies of fly ash-based geopolymers. Spectrochim. Acta A Mol. Biomol. Spectrosc. 198, 283–289. https://doi.org/10.1016/j.saa.2018.03.034.

Sabir, B.B., Wild, S., Bai, J., 2001. Metakaolin and calcined clays as pozzolans for concrete: a review. Cem. Concr. Compos. 23, 441–454. https://doi.org/10.1016/S0958-9465(00)00092-5.

Sellami, M., Barre, M., Toumi, M., 2019. Synthesis, thermal properties and electrical conductivity of phosphoric acid-based geopolymer with metakaolin. Appl. Clay Sci. 180, 5. https://doi.org/10.1016/j.clay.2019.105192.

Singhal, A., Gangwar, B.P., Gayathry, J.M., 2017. CTAB modified large surface area nanoporous geopolymer with high adsorption capacity for copper ion removal. Appl. Clay Sci. 150, 106–114. https://doi.org/10.1016/j.clay.2017.09.013.

Sitarz, M., 2008. The structure of liquation silico-phosphate glasses. J. Mol. Struct. 887, 229–236. https://doi.org/10.1016/j.molstruc.2008.02.002.

Stumm, W., Morgan, J., 2012. Aquatic Chemistry: Chemical Equilibria and Rates in Natural Waters, 3rd ed. John Wiley & Sons, pp. 516–613.

Tao, J., Pan, H., Zeng, Y., Xu, X., Tang, R., 2007. Roles of amorphous calcium phosphate and biological additives in the assembly of hydroxyapatite nanoparticles. J. Phys. Chem. B 111, 13410–13418. https://doi.org/10.1021/jp0732918.

Tchakouté, H.K., Rüscher, C.H., Kamseu, E., Andreola, F., Leonelli, C., 2017. Influence of the molar concentration of phosphoric acid solution on the properties of metakaolin-phosphate-based geopolymer cements. Appl. Clay Sci. 147, 184–194. https://doi.org/10.1016/j.clay.2017.07.036.

Tippayasam, C., Balyore, P., Thavorniti, P., Kamseu, E., Leonelli, C., Chindaprasirt, P., Chaysuwan, D., 2016. Potassium alkali concentration and heat treatment affected metakaolin-based geopolymer. Constr. Build. Mater. 104, 293–297. https://doi.org/10.1016/j.conbuildmat.2015.11.027.

Toniolo, N., Boccaccini, A.R., 2017. Fly ash-based geopolymers containing added silicate waste. A review. Ceram. Int. 43, 14545–14551. https://doi.org/10.1016/j.ceramint.2017.07.221.

Vassilev, S.V., Vassileva, C.G., 2005. Methods for characterization of composition of fly ashes from coal-fired power stations: a critical overview. Energy & Fuels 19. https://doi.org/10.1021/ef049694d.

Wagh, A.S., 2004. Chapter 14 - Chemically Bonded Phosphate Ceramic Matrix Composites. Chemically Bonded Phosphate Ceramics. Elsevier, Oxford, pp. 157–176. https://doi.org/10.1016/B978-008044505-2/50018-1.

Wagh, A.S., 2005. Chemically bonded phosphate ceramics - A novel class of geopolymers. In: Singh, J.P., Bansal, N.P., Kriven, W.M. (Eds.), Advances in Ceramic Matrix Composites X, pp. 107–116.

Wagh, A.S., 2011. Phosphate geopolymers. In: Kriven, W.M., Gyekenyesi, A.L., Wang, J. (Eds.), Developments in Strategic Materials and Computational Design II, pp. 91–103.

Wagh, A.S., Jeong, S.Y., 2003. Chemically bonded phosphate ceramics: I, a dissolution model of formation. J. Am. Ceram. Soc. 86, 1838–1844. https://doi.org/10.1111/j.1151-2916.2003.tb03569.x.

Wang, Y.-S., Alrefaei, Y., Dai, J.-G., 2019a. Silico-aluminophosphate and alkali-aluminosilicate geopolymers: a comparative review. Frontiers in Materials 6. https://doi.org/10.3389/fmats.2019.00106.

Wang, Y.-S., Alrefaei, Y., Dai, J.-G., 2019b. Improvement of early-age properties of silico-aluminophosphate geopolymer using dead burnt magnesia. Constr. Build. Mater. 217, 1–11. https://doi.org/10.1016/j.conbuildmat.2019.05.050.

Wang, Y.-S., Alrefaei, Y., Dai, J.-G., 2020. Influence of coal fly ash on the early performance enhancement and formation mechanisms of silico-aluminophosphate geopolymer. Cem. Concr. Res. 127 https://doi.org/10.1016/j.cemconres.2019.105932.

Wang, Y.S., Provis, J.L., Dai, J.G., 2018. Role of soluble aluminum species in the activating solution for synthesis of silico-aluminophosphate geopolymers. Cem. Concr. Compos. 93, 186–195. https://doi.org/10.1016/j.cemconcomp.2018.07.011.

Wikholm, N.W., Beebe, R.A., Kittelberger, J.S., 1975. Kinetics of the conversion of monetite to calcium pyrophosphate. J. Phys. Chem. 79, 853–856. https://doi.org/10.1021/j100575a017.

Williams, R.P., Hart, R.D., van Riessen, A., 2011. Quantification of the extent of reaction of metakaolin-based geopolymers using x-ray diffraction, scanning electron microscopy, and energy-dispersive spectroscopy. J. Am. Ceram. Soc. 94, 2663–2670. https://doi.org/10.1111/j.1551-2916.2011.04410.x.

Yan, F., Jiang, J., Tian, S., Liu, Z., Shi, J., Li, K., Chen, X., Xu, Y., 2016. A green and facile synthesis of ordered mesoporous nanosilica using coal fly ash. ACS Sustain. Chem. Eng. 4, 4654–4661. https://doi.org/10.1021/acssuschemeng.6b00793.

Yao, Z.T., Ji, X.S., Sarker, P.K., Tang, J.H., Ge, L.Q., Xia, M.S., Xi, Y.Q., 2015. A comprehensive review on the applications of coal fly ash. Earth Sci. Rev. 141, 105–121. https://doi.org/10.1016/j.earscirev.2014.11.016.

Youssif, M.I., Mohamed, F.S., Aziz, M.S., 2004. Chemical and physical properties of $Al1-xFe_xPO_4$ alloys - part 1. Thermal stability, magnetic properties and related electrical conductivity. Mater. Chem. Phys. 83, 250–254. https://doi.org/10.1016/j.matchemphys.2003.09.025.

Zhang, Z., Wang, H., Zhu, Y., Reid, A., Provis, J.L., Bullen, F., 2014. Using fly ash to partially substitute metakaolin in geopolymer synthesis. Appl. Clay Sci. 88-89, 194–201. https://doi.org/10.1016/j.clay.2013.12.025.

Zhang, Z., Provis, J.L., Zou, J., Reid, A., Wang, H., 2016. Toward an indexing approach to evaluate fly ashes for geopolymer manufacture. Cem. Concr. Res. 85, 163–173. https://doi.org/10.1016/j.cemconres.2016.04.007.

Zhang, B., Guo, H., Yuan, P., Li, Y., Wang, Q., Deng, L., Liu, D., 2020a. Geopolymerization of halloysite via alkali-activation: dependence of microstructures

on precalcination. Applied Clay Science 185. https://doi.org/10.1016/j.clay.2019.105375.

Zhang, B., Yuan, P., Guo, H., Deng, L., Li, Y., Li, L., Wang, Q., Liu, D., 2020b. Effect of curing conditions on the microstructure and mechanical performance of geopolymers derived from nanosized tubular halloysite. Construction and Building Materials 121186. https://doi.org/10.1016/j.conbuildmat.2020.121186.

Zhang, B., Guo, H., Yuan, P., Deng, L., Liu, D., 2020c. Novel acid-based geopolymer synthesized from nanosized tubular halloysite: The role of precalcination temperature and phosphoric acid concentration. Cement and Concrete Composites 103601. https://doi.org/10.1016/j.cemconcomp.2020.103601.